Piezoelectric Materials for the DC-DC Converters Based on Piezoelectric Resonators

Mustapha Touhami, Ghislain Despesse, Thierry Hilt, Marie Bousquet, Alexandre Reinhardt, Emma Borel, Valentin Breton, Komi-Ferdinand Gneza, François Costa

Piezoelectric Materials for the DC-DC Converters Based on Piezoelectric Resonators

Mustapha TOUHAMI[1], Ghislain DESPESSE[1], Thierry HILT[1], Marie BOUSQUET[1], Alexandre REINHARDT[1], Emma BOREL[1], Valentin BRETON[1], Komi-Ferdinand GNEZA[1], François COSTA[2].

[1]CEA-Leti, Univ. Grenoble Alpes, F-38000 Grenoble, France.

[2]University Paris-Saclay, ENS Paris-Saclay, CNRS, SATIE, Université Paris Est Créteil, 94010, Créteil France.

mustapha.touhami@cea.fr

***Abstract*—This paper presents a generic representation of the six switching sequences dc-dc converters based on piezoelectric resonator. In addition, the estimation of current density and voltage limitations of lead zirconate titanate and lithium niobate resonators are given. A comparison between these piezoelectric materials is carried out. Then, we propose a lithium niobate-based piezoelectric resonator design that reduces spurious modes, while providing a quality factor of 3700 and an electromechanical coupling factor of 25.5 %. Experimental results demonstrate the operating principle for input-output voltage of 60-20 V around 6 MHz for a wide power range 2-32 W. A peak efficiency of 93.6 % is obtained at 16 W. A power density of 128 W/cm^3 for the designed resonator is reached for input-output voltage of 60-20 V.**

Keywords—Piezoelectric resonator, DC-DC converter, soft switching, power converters, Lithium Niobate, inductorless.

I. INTRODUCTION

Nowadays, the main challenge for miniaturization and integration of power converters is reducing the volume of the passive components, such as the capacitors and the inductors contained wherein. To this end, increasing the frequency enables reducing the energy converted by cycle, which allows downsizing the passives elements [1]. While, semi-conductors (GaN HEMT) offer a possibility to increase the switching frequency regarding to conventional MOSFET, reducing the volume of inductors becomes difficult by maintaining low losses and their integrations is not compatible with the actual process [2-3]. Power converters based on capacitances ensure high power density and high efficiency compared to magnetic converters, and their integration is possible. However, their efficiency decreases for a variable gain operation [4-5].

To overcome these limitations, one potential solution consists of using piezoelectric components as a replacement for the inductors and the capacitances [6]-[16]. Piezoelectric components use the converse piezoelectric effect to convert electric energy to mechanical form and the direct effect allows converting mechanical energy to electrical one. So, employing both effects enables using the piezoelectric element as electrical-mechanical-electrical transducer. Also, the piezoelectric ceramics provide an inductive behavior between their series and parallel frequency, which enables zero voltage switching (ZVS) and soft charging operations [17]-[23]. In [17]-[24], the operating principle based on piezoelectric resonators (PR) was explored and validated experimentally for high and low voltage conversion and low power levels (<200 W). These first results show a promising future for the piezo-based power converters.

Some PZT ceramics were selected for their high quality factor (Q) and their high electromechanical coupling factor (k) [17]-[19], [20], [26]. However, the PZT materials have a high dielectric constant ($\varepsilon_{33}^S/\varepsilon_0 = 1500$) which induces a high intrinsic capacitance. As a result, the current needed to charge and discharge this capacitance over a cycle becomes higher with increasing the operating frequency [19]. In [25], Lithium Niobate (LNO) was introduced as an alternative to PZT. This material provides a lower dielectric ($\varepsilon_{33}^S/\varepsilon_0 = 30$) and a higher quality factor than PZT, while it exhibits an electromechanical coupling factor similar to the PZT ceramics. Fig. 1 shows the figures of merit k^2Q for some piezoelectric materials, where, the efficiency is plotted as a function of k^2Q, considering the switching sequence presented in [20-21], and taking into account only losses due to the damping effect of the PR. The data are collected from the datasheet of the suppliers. As shown, LNO exhibits the highest k^2Q and efficiency, making it a promising alternative to PZT. The aim of this paper is to present a comparison between PZT and LNO in terms of current density and voltages operation, and presents a design of a PR based on LNO.

This paper is organized as follow: in section II, we present a generic model of dc-dc converters based on PRs for conversion cycle with six switching stages (can be also used for four switching sequences). An example of the switching sequence is given to verify the generic model. In section III, we propose an estimation of the current density as a function of frequency with the operating voltage limits. A comparison between PZT ceramics and LNO is proposed in terms of

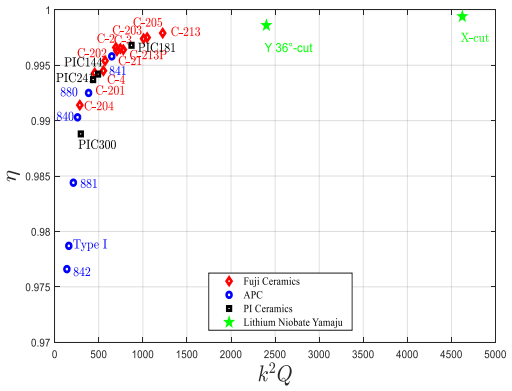

Fig. 1. Figure Of Merits of Piezoelectric Materials.

(a)

(b)

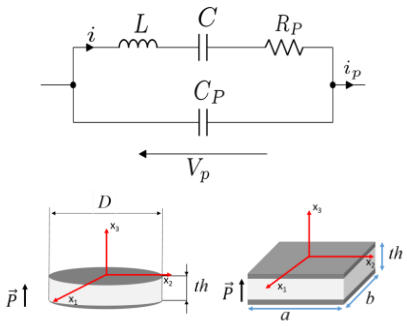

Fig. 2. (a) Butterworth Van-Dyke equivalent circuit (BVD) [27], (b) Geometry of the PR.

current density and voltage. Then, we propose a design of PR based on LNO that enables to reduce the spurious modes. In section IV, experimental results are shown to verify the performance of the dc-dc converter based on LNO resonator.

II. THE OPERATING PRINCIPLE

A. Generic conversion cycle and model

The piezoelectric resonator (PR) can be modeled using the Butterworth Van-Dyke equivalent circuit (BVD), shown in Fig. 2a. This model is composed of a LCR branch that expresses a mechanical behavior of the PR, in parallel with a capacitance C_P. Within the inductive region, located between the resonant frequency (LC) and anti-resonant frequency (L(C//C_P)), the current i in the LCR branch can be assumed sinusoidal thanks to the high quality factor of the piezoelectric materials. Therefore, the conversion cycle is composed of six stages, which alternate between connected stage (V_P = constant) and open-circuit stage (i_p =0), for operation with variable conversion gain V_{out}/V_{in} [17-25]. The connected stage allows exchanging the PR's charge with the source and/or load or zero voltage (short-circuit). The open-circuit stage enables changing the voltage level of the PR by using the soft charging/discharging of the capacitance C_P in order to turn-on the switches in ZVS mode. So, we consider a six stages conversion cycle, composed of three connected stages and three open circuit stages; where the connected stages operate at three voltage levels named V_a, V_b and V_c. These voltages can be the input voltage, the output voltage, zero voltage or a combination of the input and the output voltage. Then, we define three voltage levels {V_a, V_b, V_c}, where:

- The voltage level V_a and V_b are defined at each polarity of the current i.
- The voltage level V_c is defined at the same polarity of the current i as V_a, which results that Q_a and Q_c have the same polarity (the same sign).
- Each voltage level is defined during only a single polarity of the current i (i.e., no reactive energy).

From these considerations, the charge and energy balance (for lossless conversion cycle) are written by:

$$Q_a + Q_b + Q_c = 0 \quad (1)$$

$$Q_a V_a + Q_b V_b + Q_c V_c = 0 \quad (2)$$

By suppressing Q_b in (2) by using (1), we obtain:

$$(V_a - V_b)Q_a = (V_b - V_c)Q_c \quad (3)$$

In case $V_a > V_b$, $V_b > V_c$ is induced because Q_a and Q_c have by definition the same polarity, leading to the classification of: $\mathbf{V_a > V_b > V_c}$. As $V_a > V_c$, the current i should be positive in the half period where V_a and V_c are located, because we need to discharge the capacitance C_P to go from V_a to V_c during the open circuit stage between V_a and V_c. In the case where $V_a < V_b$, $V_b < V_c$, so, we obtain the classification of the voltages as: $\mathbf{V_a < V_b < V_c}$, and the current i should be negative, since we need to charge the capacitance C_P during the open stage between V_a and V_c. For both classifications, the voltage V_b is always defined between V_a and V_c. Therefore, we can state a *positive power flow* regarding to V_b by considering:

(a) ***A positive power flow** is **taken** under V_b*, in this case, we introduce the factor β that is equal to 1 for the classification: $V_c < V_b < V_a$.

(b) ***A positive power flow** is **provided** from V_b*, in this case, we define the factor β equal to -1 for the classification: $V_a < V_b < V_c$.

These two configurations can be merged into a single representation by using the factor β that is multiplied by the voltage V_P and the current i, which is leading to a single classification $\boldsymbol{\beta V_c < \beta V_b < \beta V_a}$. Fig. 3 shows the steady-state generic conversion cycle, with V_P the voltage across the piezoelectric and i the current. The voltage extremum V_{zvst3} (respectively V_{zvst6}) is required between the connected stage V_c and V_b (respectively between V_b and V_a) to ensure the ZVS conditions, when one end of the PR is floating. If yields that, for a given voltage levels triplet {V_1, V_2, V_3}, the construction of a conversion cycle needs firstly to identify the median voltage of {V_1, V_2, V_3}, named V_β, and the parameter β that determines the power flow as follow:

$$\begin{cases} V_\beta = \text{median}\{V_1, V_2, V_3\} \\ \beta = -\text{sign}(Q_{V_\beta}) \end{cases} \quad (4)$$

Once β is known, V_a, V_b and V_c are then immediately identified by:

$$\begin{cases} \beta V_a = \max\{\beta V_1, \beta V_2, \beta V_3\} \\ \beta V_b = \text{median}\{\beta V_1, \beta V_2, \beta V_3\} \\ \beta V_c = \min\{\beta V_1, \beta V_2, \beta V_3\} \end{cases} \quad (5)$$

The amplitude I of the current in the motional branch of the resonator is given as a function of the switching sequences:

$$I = \frac{\beta\pi}{(\alpha_b - \alpha_c) + (\alpha_a - \alpha_c)A_0} I_{out} + I_{circul} = I_{useful} + I_{circul} \quad (6)$$

where $A_0 = \frac{V_c - V_b}{V_a - V_c}$, and $I_{circul} = \frac{\beta(V_{ZVS_{t3}} - V_{ZVS_{t6}})}{2} C_P \omega$. I_{circul} is the amplitude of the circulating current required to charge and discharge the capacitance C_P over a period, this amplitude of current is required even with no load. I_{useful} is the amplitude of the current required to supply the output load, which depends on the switching sequence and the load I_{out}. The parameter α_a (respectively α_b, α_c) is defined regarding to V_a (respectively V_b, V_c) by :

$$\begin{cases} \alpha_a = -1, & if\ V_a\ contains\ (-V_{out}) \\ \alpha_a = +1, & if\ V_a\ contains\ (+V_{out}) \\ \alpha_a = 0, & otherwise \end{cases}$$

The amplitude *I* is the key parameter for the design of the PR in order to fit the requirements in terms of power and input-output voltages. The charge factor *K* in [20], can be expressed by:

$$K = \frac{(\alpha_b - \alpha_c) + (\alpha_a - \alpha_c)A_0}{2\beta} \quad (7)$$

The current amplitude *I* and the *K-factor* expressions can be validated through the examples explored in [17], [19-20]. The output current is written as a function of the switching sequence by:

$$I_{out} = \frac{P_{out}}{V_{out}} = -\left((\alpha_a - \alpha_c) + (\alpha_b - \alpha_c)\frac{V_c - V_a}{V_b - V_c}\right)\frac{Q_a}{T} \quad (8)$$

where $Q_a = \beta\frac{I}{\omega}(\cos(\omega t_3') - \cos(\omega t_4))$.

The output current is directly proportional to Q_a, which depends of the βV_a stage duration [t_3', t_4], as shown in Fig. 3. Finally, by controlling t_4, we can regulate the output current value, as illustrated in [21]. Therefore, the presented generic conversion cycle enables to:

- Give a single representation of the conversion cycle.
- Identify the unique switching sequence for a given voltage levels regarding to the conversion cycle.
- Achieve a fast calculation of the estimated current *I* and I_{out}.
- Give the feasible conversion gain ratio.

B. *Example of implementation of switching sequence*

To verify the presented generic model, we can take as an example a step-down dc-dc converter (V_{in}>V_{out}) that operates at these three voltage levels {V_{in}-V_{out}, V_{out}, 0}, explored in [20]. Therefore, V_β can be equal to V_{in}-V_{out} or V_{out}. In case of V_{out} >V_{in}-V_{out}, then V_β is equal to V_{in}-V_{out}. Therefore, a positive charge is supplied to the PR under V_β, so, the sign of $Q_{V\beta}$ is positive which leads to $\boldsymbol{\beta = -1}$. Hence, {V_a, V_b, V_c} are deduced as below:

$$\begin{cases} \beta V_a = \max\{-(V_{in} - V_{out}), -V_{out}, 0\} = 0 \\ \beta V_b = \text{median}\{-(V_{in} - V_{out}), -V_{out}, 0\} = -(V_{in} - V_{out}) \\ \beta V_c = \min\{-(V_{in} - V_{out}), -V_{out}, 0\} = -V_{out} \end{cases} \quad (9)$$

This switching sequence gives a classification of -V_{out}<-(V_{in}-V_{out}) <0, which induces to an operating condition of V_{out}<V_{in}<2V_{out}. The amplitude of the current is in this case:

$$I = \pi\frac{V_{out}}{V_{in}}I_{out} + \frac{V_{in}}{2}C_P\omega = I_{useful} + I_{circul} \quad (10)$$

where $\alpha_a = 0, \alpha_b = -1, \alpha_c = 1$.

In case of V_{out}< V_{in}-V_{out}, V_β is equal to V_{out}. Therefore, a positive charge is taken from the PR. As a result, the sign of $Q_{V\beta}$ should be negative leading to $\boldsymbol{\beta = 1}$. Thus, the triplet {V_a, V_b, V_c} are defined as follow:

$$\begin{cases} \beta V_a = \max\{V_{in} - V_{out}, V_{out}, 0\} = V_{in} - V_{out} \\ \beta V_b = \text{median}\{V_{in} - V_{out}, V_{out}, 0\} = V_{out} \\ \beta V_c = \min\{(V_{in} - V_{out}), V_{out}, 0\} = 0 \end{cases} \quad (11)$$

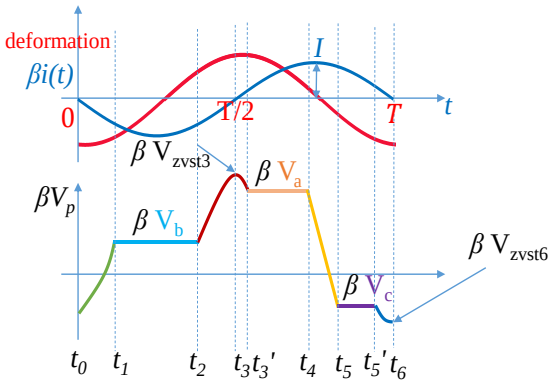

Fig. 3. Generic conversion cycle.

In this case, the voltages are classified as 0<V_{out}<V_{in}-V_{out} leading to 0<2V_{out}<V_{in}, and the amplitude *I* is then deduced directly as:

$$I = \pi\left(1 - \frac{V_{out}}{V_{in}}\right)I_{out} + \frac{V_{in}}{2}C_P\omega = I_{useful} + I_{circul} \quad (12)$$

where $\alpha_a = -1, \alpha_b = 1, \alpha_c = 0$.

The presented generic conversion cycle can be validated as well through the enumerated switching sequences shown in [19-24].

III. LITHIUM NIOBATE PR: DESIGN AND FABRICATION

A. *PR model*

The electrical parameters of the PR based on the BVD circuit (see Fig. 2a) are linked to the physical properties and geometry of the PR. Equations (13)-(16) give the electrical parameters as a function of the physical properties and geometry for an ideal rectangular plate and a disk operating in thickness extensional vibration mode [28], as shown in Fig. 2b. The BVD model can be determined as a function of the resonator proprieties and the designed geometry: the area *A=ab* (or *πD²/4* for disk shape) and the thickness *th* of the PR:

$$C_P = \varepsilon_{33}^S * \frac{A}{th} = \varepsilon_{33}^T(1 - k_{33}^2)\frac{A}{th} \quad (13)$$

$$C = \frac{8k_{33}^2 C_P}{\pi^2 - 8k_{33}^2} \quad (14)$$

$$L = \frac{th^2\rho}{8\,C_P k_{33}^2 Y_{33}^D} \quad (15)$$

$$R_P = \frac{2\pi L f_r}{Q} \quad (16)$$

where k^2_{33} is the electromechanical factor, *Q* is the quality factor of the material and illustrates the mechanical losses. ρ is the density of the material in kg/m^3, and $Y_{33}^D(N/m^2)$ is the Young's modulus of the material at constant stress. The equivalent impedance of the PR (Z_{PR}) is then given by (17):

$$Z_{PR}(f) = \frac{1}{j2\pi f C_P}\frac{R_P + i2\pi Lf\left(1 - \left(\frac{fr}{f}\right)^2\right)}{R_P + i2\pi Lf\left(1 - \left(\frac{far}{f}\right)^2\right)} \quad (17)$$

where f_r is the resonant (series) frequency and f_{ar} is the anti-resonant (parallel) frequency [17].

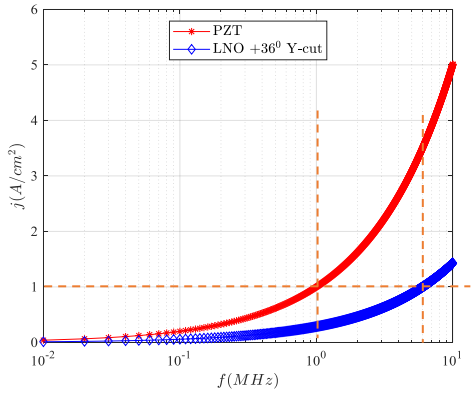

Fig. 4. The evolution of the current density as a function of the frequency for PZT and LNO.

B. *Density of the current and limitations*

As demonstrated in [19], [29], the amplitude of the current I is mainly related to the area of the PR in thickness extensional mode which is therefore the key element for designing the PR. However, this current density $j(f)$ is given for a fixed operating frequency. By using the experimental results in [19], the current density can be empirically estimated by (18) for PZT ceramics:

$$j(f) = j_0 * 10^{0.7 \log_{10}\frac{f}{f_0}} \tag{18}$$

where, $j_0 = 1\ A/cm^2 @\ f_0 = 1\ MHz$ for the PZT C-213 from Fuji Ceramics. This expression states that the current density scales by a factor five per frequency decade. Assuming that the current density of LNO + 36° Y-cut evolves according to the same law, Fig. 4 shows the evaluation of the current density as a function of the frequency. For LNO, we consider the current density of $j_0 = 1\ A/cm^2$ at 6 MHz that was reached in [25]. Consequently, LNO provides a lower current density than PZT at same frequency. Assuming the current density expression (18), we can then derive the expression of the maximum voltage applied $U_{max}(f)$ on the PR when all the amplitude of I is used to charge and discharge the capacitance C_P (i.e., I=I_{circul}), and when the operating frequency is near to the anti-resonant frequency (open circuit operation). Therefore, the voltage $U_{max}(f)$ gives an upper limit of using the PR as function of f even without load, where U_{max} decreases linearly with $1/f$ (i.e., $U_{max}\ \alpha\ 1/f$ as $j\ \alpha f$).

$$U_{max}(f = f_{ar}) = \frac{I(f_{ar})}{2\pi C_p f_{ar}} = \frac{j(f_{ar})}{2\pi f_{ar}^2 \gamma} \tag{19}$$

where $\gamma = \varepsilon_{33}^S \sqrt{4\rho/Y_{33}^D}$, as $Y_{33}^D = 4\rho f_{ar}^2 th^2$, [28].

However, for an output load, the current I_{useful} is not zero (i.e., I_{useful} is the amplitude of the current required to supply the load). It depends on the output load, as seen in (6). So, we need to reduce I_{circul} (i.e., I_{circul} is the amplitude of the current required to charge and discharge the C_P over a period), because I is constant as it is determined by the physical proprieties and the geometry of the PR. Thus, to reduce I_{circul}, we can reduce the voltage applied on the PR, (6). Therefore, we define $U_{min}(f)$ that gives the minimum circulating current while I_{useful} is maximized, which leads to an operating frequency that is taken slightly higher than the resonant frequency, because if f=f_r, Z_{PR} is then equal to R_P. Consequently, the PR is only resistive and no energy is transferred to load. Therefore, we define a phase shift δ_{PR} caused by the mechanical losses near f_r, while the PR still inductive, which is given by (20), obtained from the impedance Z_{PR}.

TABLE I. Comparative between LNO and PZT at the same current density.

	Nt (MHz.mm)	*c(mm)*	*f_0 (MHz)*	*j_0(A/cm²)*
LNO+36°Y-cut	3.3	0.5	6.6	~1
PZT	2	2	1	~1

$$\delta_{PR} = \pi - \tan^{-1}\frac{2\pi Lf\left(1-\left(\frac{fr}{f}\right)^2\right)}{R_P} + \tan^{-1}\frac{2\pi Lf\left(1-\left(\frac{far}{f}\right)^2\right)}{R_P} \tag{20}$$

For a high quality factor material (i.e., $-2\pi Lf(1-(f_{ar}/f)^2) \gg R_P$), the equation (20) can be simplified into a function of Q and $\lambda = \frac{f}{fr}$ assuming λ>1:

$$\tan\delta_{PR} = \frac{1}{Q\lambda\left(1-\left(\frac{1}{\lambda}\right)^2\right)} \tag{21}$$

By imposing a phase shift (loss rate $\tan\delta_{PR}$)), we can deduce λ by solving the following equation:

$$\lambda^2 - (Q\tan\delta_{PR})^{-1}\ \lambda - 1 = 0 \tag{22}$$

Once λ is solved, we can determine U_{min} by computing:

$$U_{min}(\lambda f_r) = I(\lambda f_r) Z_{PR}(\lambda f_r) \tag{23}$$

In Fig. 5, we have plotted the maximum voltage U_{max} on the PR when the maximum current I that the piezoelectric can sustain is only a circulating current, and the minimum voltage U_{min} that enable to reach that same maximum current I. That last one operating voltage minimizes the circulating current while maximizing the useful current. This plot is done for a PZT C-213 operating in thickness mode, considering a quality factor of 2000 and a loss rate of 2%. The filled area corresponds to the operating area where the physical maximum current density is reachable and not exceeded. Indeed, for a given frequency, increasing the voltage increases the circulating current while the useful current decreases as the current amplitude I is constant, since I depends only on the material's proprieties. Also, the filled area decreases with the quality factor and increases with increasing the loss rate. This plot can be crossed with the dielectric strength of the material (i.e., U=$E_{bd}N_t/f$, where Nt is the frequency thickness constant of the piezoelectric ceramic). As shown, when increasing the frequency, the voltage decreases, what limits the operating points in terms of voltage (for instance: at 10 MHz , U=[0.5 V, 25 V]), limiting the downsizing of the PR, due to the high dielectric constant of PZT, (19). Therefore, using LNO with a lower dielectric constant, a higher quality factor and coupling factor could be an alternative at higher frequency and high voltage operation. Indeed, as shown in Fig. 6, LNO voltage operating range is shift in higher voltage than the PZT (for instance, at 10 MHz, U= [14 V, 258 V]), which illustrates a good potential of utilization at high operating frequency (>1 MHz) for usual < 600 V voltage range operation.

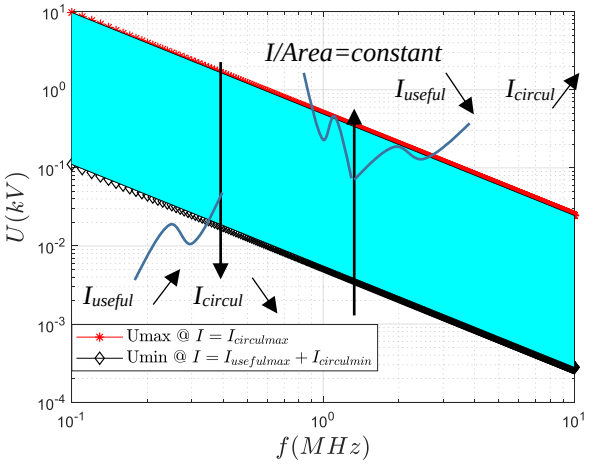

Fig. 5. Voltage limits for PZT C-213, with Q = 2000 and tan δ_{PR} = 2 %.

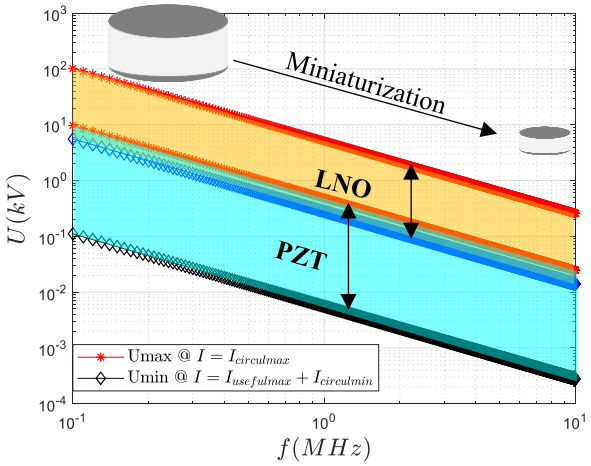

Fig. 6. Voltage limits comparison between PZT C-213 in cyan color and for LNO +36°Y-cut in gold color, for Q=2000 and tan δ_{PR} = 2 %.

To sum up, these plots enable to design a PR regarding to operating conditions {*P*, *f* and *V*}, by considering a distribution between the circulating current (*f*, *V*) and the useful current (*P or* I_{out}).

C. Lithium Niobate resonator: Design and fabrication

Lithium niobate is an anisotropic material [30]. Therefore, the piezoelectric constant (d_{33} in C/N) and the dielectric constant of the material depend on the orientation of the piezoelectric crystal, as illustrated in [31]. In this work, we have selected lithium niobate +36°Y-cut plates (promoting a quasi-extensional vibration mode) because it offers a good compromise between obtaining a high piezoelectric electromechanical coupling and a low dielectric constant (i.e., *low* C_P *leading to low* I_{circul}*)*. Also, we aim to fabricate a PR for a low voltage operation (< 100 V) and exhibiting a resonant frequency around 6 MHz. The PR is fabricated from a double-side polished 4 inch commercial black-LNO +36°Y-cut wafer with a thickness of 0.5 mm ± 20µm (black wafers allow reducing the pyroelectric effect of the material during the fabrication process), from the supplier Yamaju Ceramics. On both sides of the wafer, 2 µm-thick aluminum electrodes were deposited by evaporation and then patterned by wet etching. Fig. 7 shows the fabricated wafer after wafer dicing, with two resonator shapes. Deported electrodes are used at the top and bottom of each samples for the electrical contacts with the PCB board, in order to reduce the impact of the mechanical fixtures on the PR's mechanical behavior. The two types of devices have the same active area, which is ~5 cm².

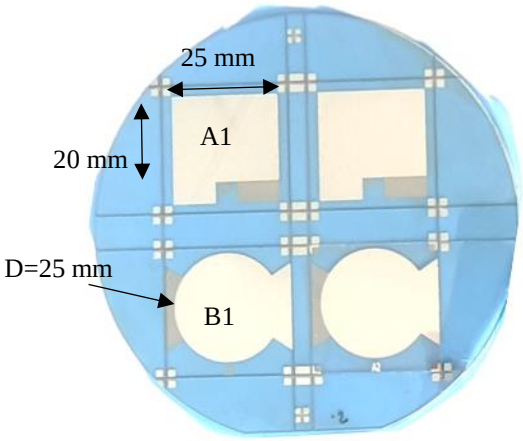

Fig. 7. Fabricated wafer LNO +36°Y-cut.

D. Impedance plot

Fig. 8 shows the impedances of the PR obtained by using an impedance analyzer. For the measurement, the PR have been mounted on PCB as shown in Fig. 9a. The electrical contacts are made by using wire bonding at the top and bottom of the deported electrodes. In addition, the measured impedances of the PR are compared to the theoretical model (the fundamental mode) that is plotted in dashed curves, revealing a good agreement with the fabricated prototypes. However, as shown in the Fig. 8a, the rectangular PR exhibits spurious modes within the inductive region due to lateral vibration modes, which create a discontinuity in terms of the

TABLE II. Electrical model of the PR for the disk shape.

parameters	Calculated	Measured
$\varepsilon_{33}^{S}/\varepsilon_0$	36.64	37.4
C_P	315pF	325pF*
C	72.2pF	84.5pF
L	8.75µH	7.6µH
R_P	33mΩ	80 mΩ**
f_r	6.3MHz	6.281MHz
f_{ar}	7.03MHz	7.1MHz
k_t^2***	0.24	0.255
Q	10^4****	3700
$k_t^2 Q$	2400	955

*** C_P=325pF is measured at outside of the resonant frequency *3fr* around 18MHz. The measurement of C_P is provided with an accuracy of +/-10%.**R_P is measured at the series frequency f_r.***k_t is the coupling factor for disk shape resonator for thickness mode and taken insteade of k_{33}.****Q is not given by the supplier, so we have approximated Q by $Q = 10^{11}/f_r$ [30].**

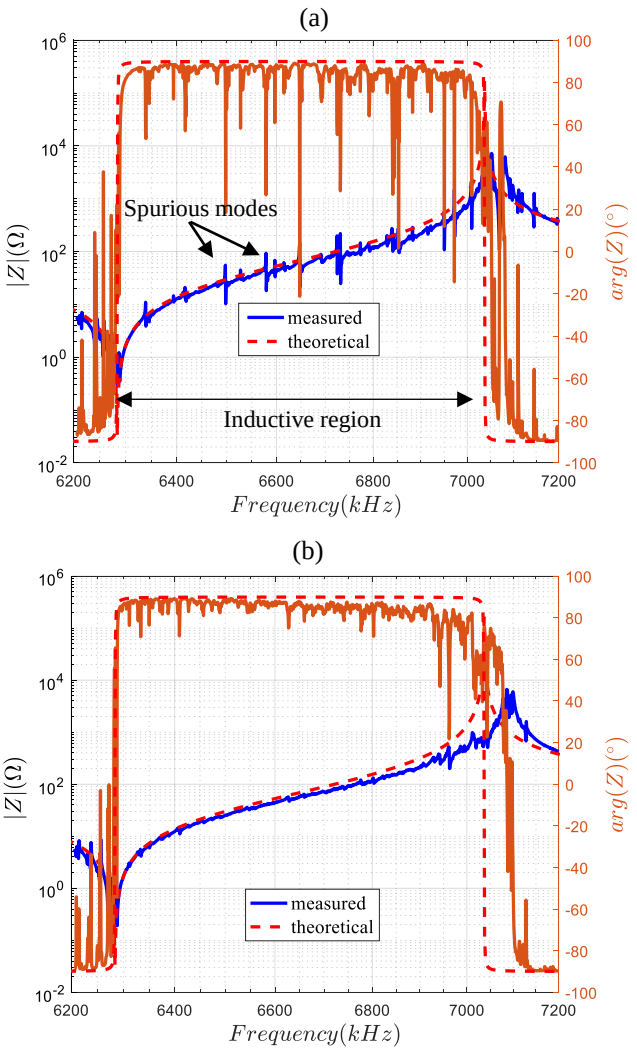

Fig. 8. PR's impedance between its resonance and anti-resonance for: (a) disk with D=25mm and th=0.521mm, (b) Rectangular with a=20mm, b=25mm and th=0.521mm.

operating points as the power is depending on the frequency [24]-[25]. Nevertheless, these spurious modes can be attenuated by using a disk shape PR. Indeed, in Fig. 8b, the disk shape resonator exhibits a lower spurious mode content in the inductive region.

From the plotted impedance and using (24)-(27), we have extracted the equivalent electrical circuit for the disk resonator, shown in TABLE II. Indeed, TABLE II shows a good accuracy between the equivalent electrical model parameters obtained from the theoretical equations and from the experimental impedance. The designed PR provides a high quality factor of 3700 and high coupling of 25.5 %, which gives k^2Q of 955.

$$k_{33}^2 = \frac{\pi}{2}\frac{f_r}{f_{ar}}\cot\left(\frac{\pi}{2}\frac{f_r}{f_{ar}}\right) \quad (24)$$

$$C = \frac{8k_{33}^2 C_P}{\pi^2 - 8k_{33}^2} \quad (25)$$

$$L = \frac{1}{4\pi^2 C f_r^2} \quad (26)$$

$$Q = \frac{2\pi L f_r}{R_p} \quad (27)$$

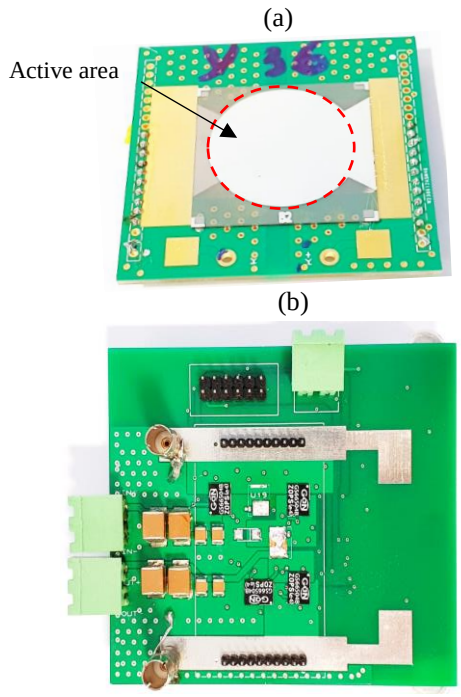

Fig. 9. Photograph of the mounted PR on PCB phi-board (a), and of the circuit board (b).

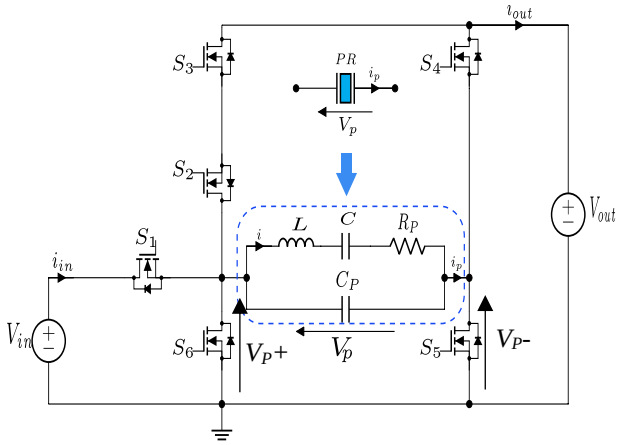

Fig. 10. Circuit topology.

IV. Experimental Results

In this part, we have integrated the fabricated PR into a dc-dc converter. The prototype is described and experimental results are exhibited to validate the operation of LNO based PR in dc-dc converters.

A. Topology and setup

The topology of the dc-dc step-down converter is presented in [19], and shown in Fig. 10. In this paper, we focus on the switching sequence presented in section II.B and [20]. Therefore, only S1, S2, S4 and S5 are used to operate with the switching sequence {V_{in}-V_{out}, 0, V_{out}}. Fig. 9 presents the mounted PR on PCB phi-board and the main circuit board. The circuit is based on two layers of copper of 1 oz and a size of 11x9 cm². The GS66504B was taken for the switches with the gate driver SI8271. The switches are driven by V_{GS}=+5 V/-2 V. The equivalent model of the PR is

shown in TABLE II. The PWMs are generated by a PLL clock implemented on FPGA (XC7A35TICSG324) with a precision of 1 % of the resonant period, so, the angular stages are conserved while the frequency is tuned. The timings are pre-calculated by using the analytical model presented in [19], [24] and solved at the center frequency between resonant and anti-resonant frequency, and then tuned to ensure soft switching and soft charging.

(a): V_{in}= 60 V, V_{out}= 20 V, P_{out} = 4 W+/-10%, f = 6.632 MHz, η = 72 %.

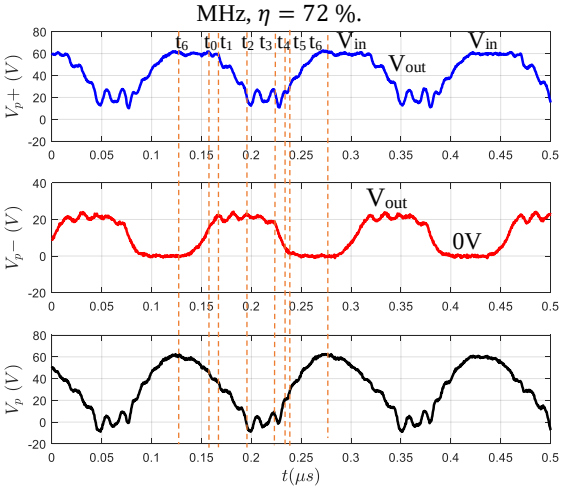

(b): V_{in}= 60 V, V_{out}=20 V, P_{out} = 13.2 W+/-10%, f = 6.432 MHz, η = 92.3 %.

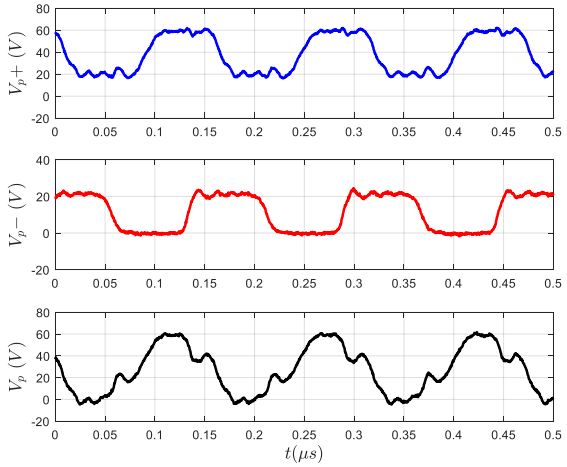

(c): V_{in}= 60 V, V_{out}= 20 V, P_{out} = 28 W+/-10%, f= 6.355 MHz, η = 91 %.

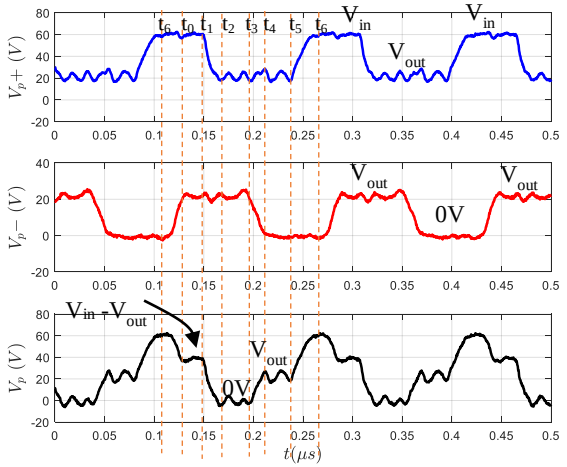

Fig. 11. Experimental waveforms of PR'voltage at differents power levels for switching sequence {V_{in}-V_{out}, 0, V_{out}}.

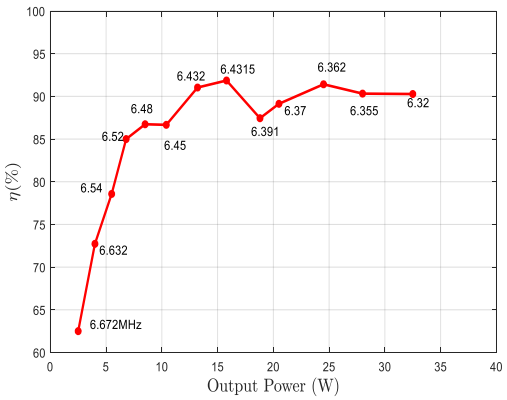

Fig. 12. Efficiency Vs. Output Power: V_{in}=60 V and V_{out}=20 V.

B. *Waveforms*

As mentioned before, we use the switching sequence {V_{in}-V_{out}, 0, V_{out}}, whose theoretical waveforms are shown in [20], [25], with corresponding timing {t_0...t_6} shown in Fig. 3. Fig. 11 shows the evolution of the experimental waveforms of the voltage across the PR at different power levels, and for an input voltage of 60 V and a gain ratio of 1/3. V_{P+} and V_{P-} are the voltages at the ends of the PR (as shown in Fig. 10), and V_P is the voltage across the PR determined by $V_{P=}$ $V_{P+}-V_{P-}$. As shown in Fig. 11, voltage oscillations can be observed due to the parasitic inductance in series with the PR. These oscillations can be reduced by optimizing the routing on the PCB. By increasing the power, the frequency decreases and the timing of the connected stages increases while the open stages decrease. Indeed, for P_{out} = 4 W, the connected stages time-duration is very low as the amplitude of current I is low. However, by increasing the output power, the time duration of open stages decreases as I increases, which enables changing voltage levels briefly. As illustrated in Fig. 12, the PR can operate at low (P_{out} = 2 W) and high power (P_{out} = 32 W), which gives a wide range of operating power. Indeed, for the PR based on LNO that has been used in [25], the minimum output power was 18 W, as the designed PR in this case provided spurious modes in the inductive region, limiting the power range operation.

C. *Efficiency*

Fig. 12 shows the efficiency as function of the output power for a wide power range of [2- 32 W] for input-output voltages of 60-20 V. As illustrated, the power converter shows a good efficiency; with a peak efficiency of 93.6% reached for 16 W. The efficiency is lower than expected, due to losses induced by turning-on the switches, which are not being turned on exactly with a ZVS mode. Indeed, the timing control has a precision of 1 % of the period deriving from a PLL clock of 600 MHz, for an operating frequency around 6 MHz. This precision is however not enough to ensure a perfect ZVS mode and soft charging. Furthermore, the voltage oscillations make it difficult to turn-on the switches with ZVS modes. Yet, the efficiency is higher than 85 % over a wide power range and expected higher with an optimized control.

V. CONCLUSION

In this paper, we have presented a generic model of dc-dc converters based on piezoelectric resonators. Then, we have

proposed an estimation of the current density and voltage operating limits of PZT and LNO. A design of PR based on LNO is proposed, achieving a quality factor of 3700 and a coupling factor of 25.5 %. In addition, the proposed design enables to reduce spurious modes which allows to operate on a wide output power range. The designed PR enables to operate for an output power range of 2-32 W for input-output voltage of 60-20 V. A peak efficiency of 93.6 % is achieved for an output power of 16 W. As demonstrated, LNO enables operation at higher frequency and/or higher voltage compare to PZT material while ensuring high coupling and quality factors. Also, the designed PR provides a power density of 128 W/cm² for 60-20 V input-output operation. The study of this material will be deepened in future work to reach its limits.

ACKNOWLEDGEMENT

This work is supported by Carnot National Institutes and CEA Leti.

REFERENCES

[1] D. J. Perreault *et al.*, "Opportunities and Challenges in Very High Frequency Power Conversion," *2009 Twenty-Fourth Annual IEEE Applied Power Electronics Conference and Exposition*, 2009, pp. 1-14, doi: 10.1109/APEC.2009.4802625.

[2] C. R. Sullivan, B. A. Reese, A. L. F. Stein and P. A. Kyaw, "On size and magnetics: Why small efficient power inductors are rare," *2016 International Symposium on 3D Power Electronics Integration and Manufacturing (3D-PEIM)*, 2016, pp. 1-23, doi: 10.1109/3DPEIM.2016.7570571.

[3] C. R. Sullivan, D. V. Harburg, J. Qiu, C. G. Levey and D. Yao, "Integrating Magnetics for On-Chip Power: A Perspective," in *IEEE Transactions on Power Electronics*, vol. 28, no. 9, pp. 4342-4353, Sept. 2013, doi: 10.1109/TPEL.2013.2240465.

[4] M. D. Seeman and S. R. Sanders, "Analysis and Optimization of Switched-Capacitor DC–DC Converters," in *IEEE Transactions on Power Electronics*, vol. 23, no. 2, pp. 841-851, March 2008, doi: 10.1109/TPEL.2007.915182.

[5] M. S. Makowski and D. Maksimovic, "Performance limits of switched-capacitor DC-DC converters," Proceedings of PESC '95 - Power Electronics Specialist Conference, 1995, pp. 1215-1221 vol.2, doi: 10.1109/PESC.1995.474969.

[6] Jian Lu, Yi Zhang, T. Itoh and R. Maeda, "Design, fabrication, and integration of piezoelectric MEMS devices for applications in wireless sensor network," 2011 Symposium on Design, Test, Integration & Packaging of MEMS/MOEMS (DTIP), 2011, pp. 217-221.

[7] M. Ekhtiari, Z. Zhang and M. A. E. Andersen, "State-of-the-art piezoelectric transformer-based switch mode power supplies," IECON 2014 - 40th Annual Conference of the IEEE Industrial Electronics Society, 2014, pp. 5072-5078, doi: 10.1109/IECON.2014.7049271.

[8] L. Wang, Q. Wang, M. Khanna, R. P. Burgos, K. D. T. Ngo and A. V. Carazo, "Design and Control of Tunable Piezoelectric Transformer Based DC/DC Converter," 2018 IEEE Energy Conversion Congress and Exposition (ECCE), 2018, pp. 5987-5993, doi: 10.1109/ECCE.2018.8557856.

[9] A. M. Flynn and S. R. Sanders, "Fundamental limits on energy transfer and circuit considerations for piezoelectric transformers," in IEEE Transactions on Power Electronics, vol. 17, no. 1, pp. 8-14, Jan. 2002, doi: 10.1109/63.988662.

[10] M. S. Rßdgaard, T. Andersen and M. A. E. Andersen, "Empiric analysis of zero voltage switching in piezoelectric transformer based resonant converters," 6th IET International Conference on Power Electronics, Machines and Drives (PEMD 2012), 2012, pp. 1-6, doi: 10.1049/cp.2012.0217.

[11] E. L. Horsley, A. V. Carazo, N. Nguyen-Quang, M. P. Foster and D. A. Stone, "Analysis of Inductorless Zero-Voltage-Switching Piezoelectric Transformer-Based Converters," in IEEE Transactions on Power Electronics, vol. 27, no. 5, pp. 2471-2483, May 2012, doi: 10.1109/TPEL.2011.2169431.

[12] R. L. Lin, F. C. Lee, E. M. Baker and D. Y. Chen, "Inductor-less piezoelectric transformer electronic ballast for linear fluorescent lamp," APEC 2001. Sixteenth Annual IEEE Applied Power Electronics Conference and Exposition (Cat. No.01CH37181), 2001, pp. 664-669 vol.2, doi: 10.1109/APEC.2001.912440.

[13] J.-H. Park, G.-S. Seo, B. Cho, and K.-P. Yi, "A resonant-type stage-up dc/dc converters with piezoelectric transducers," *The Transactions of the Korean Institute of Power Electronics*, vol. 14, 01 2009.

[14] S. Moon and J.-H. Park, "High power DC–DC conversion applications of disk-type radial mode Pb (Zr, Ti)O_3 ceramic transducer," *Japanese Journal of Applied Physics*, vol. 50, no. 9, p. 09ND20, sept 2011.

[15] G. Seo, J. Shin, and B. Cho, "A magnetic component-less series resonant converter using a piezoelectric transducer for low profile application," in *The 2010 International Power Electronics Conference - ECCE ASIA -*, 2010, pp. 2810–2814.

[16] B. Pollet, G. Despesse, and F. Costa, "A new non-isolated low-power inductorless piezoelectric dc–dc converter," *IEEE Transactions on Power Electronics*, vol. 34, no. 11, pp. 11002–11013, 2019.

[17] B. Pollet, G. Despesse and F. Costa, "A New Non-Isolated Low-Power Inductorless Piezoelectric DC–DC Converter," in IEEE Transactions on Power Electronics, vol. 34, no. 11, pp. 11002-11013, Nov. 2019, doi: 10.1109/TPEL.2019.2900526.

[18] S. Ghandour, G. Despesse and S. Basrour, "Design of a new MEMS DC/DC voltage step-down converter," Proceedings of the 8th IEEE International NEWCAS Conference 2010, 2010, pp. 105-108, doi: 10.1109/NEWCAS.2010.5603714.

[19] M. Touhami, G. Despesse and F. Costa, "A New Topology of DC-DC Converter Based On Piezoelectric Resonator," 2020 IEEE 21st Workshop on Control and Modeling for Power Electronics (COMPEL), 2020, pp. 1-7, doi: 10.1109/COMPEL49091.2020.9265767.

[20] J. D. Boles, J. J. Piel and D. J. Perreault, "Enumeration and Analysis of DC–DC Converter Implementations Based on Piezoelectric Resonators," in IEEE Transactions on Power Electronics, vol. 36, no. 1, pp. 129-145, Jan. 2021, doi: 10.1109/TPEL.2020.3004147.

[21] M. Touhami, G. Despesse, F. Costa and B. Pollet, "Implementation of Control Strategy for Step-down DC-DC Converter Based on Piezoelectric Resonator," 2020 22nd European Conference on Power Electronics and Applications (EPE'20 ECCE Europe), 2020, pp. 1-9, doi: 10.23919/EPE20ECCEEurope43536.2020.9215910.

[22] W. D. Braun *et al.*, "Optimized Resonators for Piezoelectric Power Conversion," in *IEEE Open Journal of Power Electronics*, vol. 2, pp. 212-224, 2021, doi: 10.1109/OJPEL.2021.3067020.

[23] J. D. Boles, E. Ng, J. H. Lang and D. J. Perreault, "High-Efficiency Operating Modes for Isolated Piezoelectric-Transformer-Based DC-DC Converters," *2020 IEEE 21st Workshop on Control and Modeling for Power Electronics (COMPEL)*, Aalborg, Denmark, 2020, pp. 1-8.

[24] L. de Araujo Pereira, A. Morel, M. Touhami, T. Lamorelle, G. Despesse and G. Pillonnet, "Operating Frequency Prediction of Piezoelectric DC-DC converters," in *IEEE Transactions on Power Electronics*, doi: 10.1109/TPEL.2021.3115182K.

[25] W. D. Braun et al., "Optimized Resonators for Piezoelectric Power Conversion," in IEEE Open Journal of Power Electronics, vol. 2, pp. 212-224, 2021, doi: 10.1109/OJPEL.2021.3067020.

[26] M. Vincent, D. Ghislain, C. Sebastien and M. Xavier, "A new topology of resonant inverter including a piezoelectric component," 2021 23rd European Conference on Power Electronics and Applications (EPE'21 ECCE Europe), 2021, pp. P.1-P.10.

[27] K. S. Van Dyke, "The Piezo-Electric Resonator and Its Equivalent Network," in Proceedings of the Institute of Radio Engineers, vol. 16, no. 6, pp. 742-764, June 1928, doi: 10.1109/JRPROC.1928.221466.

[28] J. Erhart, P. Půlpán, and M. Pustka, "Piezoelectric Ceramic Resonators". Springer, 2017.

[29] J. D. Boles, J. E. Bonavia, P. L. Acosta, Y. Ramadass, J. Lang and D. J. Perreault, "Evaluating Piezoelectric Materials and Vibration Modes for Power Conversion," in IEEE Transactions on Power Electronics, doi: 10.1109/TPEL.2021.3114350.

[30] H. Bhugra and G.Piazza, "Piezoelectric MEMS Resonators". Springer, 2017.

[31] Yue Wang and Yijian Jiang, "Dielectric and piezoelectric anisotropy of lithium niobate and lithium tantalate single crystals," 2009 18th IEEE International Symposium on the Applications of Ferroelectrics, 2009, pp. 1-4, doi: 10.1109/ISAF.2009.5307547.